Deformation Behavior of a Roll-Cast Layered-Silicate/Lamellar Triblock Copolymer Nanocomposite

Yung-Hoon Ha and Edwin L. Thomas*

Department of Materials Science and Engineering, Massachusetts Institute of Technology, Cambridge, Massachusetts 02139

Received December 19, 2001

ABSTRACT: We have produced layered-silicate−lamellar triblock copolymer nanocomposites possessing a uniaxial texture. Solution blending of the layered-silicate suspension with a block copolymer solution and subsequent roll-casting or static casting and annealing resulted in a partially immiscible and intercalated structure with only a low degree of exfoliation. Isotropic polygranular nanocomposite samples prepared by static solution casting exhibit increase in modulus, higher yield stresses, earlier onset of strain hardening, increased strain hardening rate, and higher residual strains upon unloading with increasing layered-silicate content. In-situ and ex-situ deformation studies were performed along various directions on roll-cast nanocomposite samples to elucidate the effects of anisotropic particles upon deformation of the globally textured nanocomposite system. Deformation parallel to the roll-cast direction shows an earlier onset of strain hardening with modest increases in the modulus for particle-loaded films compared to that of the roll-cast neat triblock. The evolution of the triblock copolymer microstructure with applied strain shows the breakup of the glassy polystyrene domains as was found for pure triblock copolymers. Upon unloading, the residual strain increases with increased loading content, and the unloaded SAXS patterns show a distribution of lamellar spacings, suggesting significant unloading effects due to the presence of the clay layers. Deformation perpendicular to the texture axis shows a dramatic increase in the tensile modulus compared to the unreinforced material. The evolution of microstructure with strain in this direction is reminiscent of a neat triblock copolymer where at high strains (∼100%) the layers kink to form the chevron morphology, and the lamellar normals continue to rotate away from the deformation direction with increasing strain at constant lamellar spacing. Unlike a pure triblock copolymer, however, the chevron morphology remains locked in place upon unloading due to the presence of the layered-silicate particles.

Introduction

Layered-silicates have been incorporated into various homopolymers as a means for improving materials properties.[1−8] In general, the dramatic increase in the resulting hybrid properties at low loading content (<5 wt %) is attributed to the exfoliated and intercalated structure of the clay, whereas loading of the same amount of nonexfoliated particles has not shown significant alteration of the resulting composite properties. The intercalated and exfoliated homopolymer−clay structures are termed "nanocomposites" due to the novel properties arising from the interactions between the matrix and the filler material on the nanometer size scale.

Thermoplastic elastomers can also be considered as a type of nanocomposite system. Triblock glassy−rubbery−glassy copolymer thermoplastic elastomers can be processed into near-single-crystal texture structures and used as a model system to study the morphology evolution during deformation.[9−25] The ability to form highly textured samples using various combinations of temperature and flow fields is critical for elucidating the detailed microstructural basis for their mechanical properties. Cohen et al.[19,20] have recently investigated the mechanisms of deformation in well-oriented near-single-crystal roll cast samples of a lamellar styrene−butadiene−styrene (SBS) triblock copolymer tested along various directions with respect to the lamellar normal and as a function of temperature.

Relatively little work has been devoted to combining clay and block copolymer materials to produce a hierarchical nanocomposite structure. The first report of a block copolymer−clay nanocomposite appears to be that of Laus et al.,[26] who studied melt (120 °C) processed blends of a SBS triblock containing 30 wt % PS (total molecular weight of 70 000) both with an organically modified montmorillonite clay and with an unmodified clay for 10, 20, and 30 wt % clay loadings. Given the polymer composition and molecular weight, the material was processed well below the order−disorder transition temperature (ODT). The unmodified clay composites showed almost no change in properties whereas for the modified clay, the plateau modulus and PS domain glass transition increased significantly with clay content and with longer annealing times (120 °C). X-ray scattering showed an increase in the silicate layer spacing for the modified clays, indicating some intercalation by the triblock into the clay particles. No further morphological characterization of the samples was done but presumably the PS formed cylindrical microdomains typical of triblocks of this composition. The glass transition temperature of the PB was unaffected by the addition of either type of clay whereas the T_g of the PS as measured by DSC increased systematically only with organically modified clay content, indicating that the clay was preferentially localized in the PS regions. No large strain behavior was investigated, but the authors concluded that the addition of clay would help raise the application temperatures for thermoplastic elastomers.

Galanti et al.[27] have also studied melt-processed blends of a cylindrical microdomain (31 wt % styrene) triblock copolymer (total molecular weight of 166 000) with a montmorillonite modified by a coupling agent, isopropyl tristearoyl titanate. They showed that the

10.1021/ma012210h CCC: $22.00
Published on Web 04/19/2002

addition of the organophilic clay allows lower mixing temperatures and smaller torques as compared to the unmodified clay. X-ray analysis unfortunately was not carried out to show whether the samples have been intercalated or exfoliated. DMTA analysis shows that whereas the PB glass transition temperature does not change, the PS glass transition temperature fluctuates from sample to sample, without a strong trend with clay content. The storage modulus increases with increasing clay content for both the PB and the PS. Despite the fact that the cylindrical PS domain morphology may preclude the insertion of the large clay layers into the PS domains, suggesting few interactions between the clay and the PS components, the 50% heat deflection temperature of the composite system was chosen as the PS glass transition temperature. The samples with the highest amount of the organic titanate show the best dimensional stability. The authors do not detail the processing history of the samples for mechanical testing which may impart orientation, and no consideration was given to the possible anisotropy of the system during tensile testing. Nevertheless, Galanti et al.[27] show that the tensile strength possesses a maximum depending on the percentage of clay and the percentage of the organophilic modifier in the clay and that the elongation to break increases with increasing clay content.

By using a low molecular weight diblock, Ren et al.[28] were able to blend organically modified montmorillonite at 0−10 wt % loading above the copolymer ODT. The authors investigated the linear viscoelastic response of the 17 000 molecular weight, 44 wt % styrene lamellar PS/PI diblock−clay composites. X-ray studies of the composites show an intercalated structure whereas the same clay dispersed in isoprene homopolymer does not show any noticeable shift in the clay gallery height. Rheological studies show that while the unfilled PS/PI diblock exhibits liquidlike behavior (consistent with a disordered state above the ODT), the clay filled hybrids begin to show solidlike behavior in the low-frequency regime with increasing loading content. They attribute this to the physical jamming of the anisotropic particles and not to the shift in the ODT of the clay-containing block copolymer hybrids.

Dumitru et al.[29] have studied the effect of adding a very large amount of organically modified clay (60 wt %) in a SBS triblock containing 27.5 wt % styrene. Samples were produced by injection molding. They studied the effects of isosteric acid (ISA) and maleinized polybutadiene (MPB) compatibilized clay on the ultimate tensile properties and on the shear viscosities of the hybrid system, although any possible block copolymer orientation development through injection molding was not considered. Furthermore, the organophilic substitution was performed in toluene, which suggests the cation-exchange reaction may not occur and that only a monolayer of the modifiers are adsorbed onto the tactoid surfaces. No morphological characterization of the clay or the block copolymer was performed. Dumitru et al. find surprisingly that, relative to the untreated SBS, the addition of 60 wt % of ISA modified clay leads to *lower* melt viscosities and enhanced strain-induced crystallization and that the addition of MPB-modified clay leads to decreased strain-induced crystallization and hence reduced ultimate tensile properties. No explanation for these unexpected effects was provided.

Lim and Park[30] have studied the effect of melt blending a small amount of organophilic clay (3−5 wt %) in a 40 wt % styrene 180 000 molecular weight SBS and epoxidized butadiene block SBS (5, 10, and 20 wt % epoxy relative to the butadiene block). They maintain that only the styrenic blocks intercalate into the clay layer with partial intercalation of the butadiene block only when it is epoxidized. Rheological studies show, similar to Ren et al.,[28] that despite the low loading content, both the storage moduli and the complex viscosities of the nanocomposite increase relative to the neat triblock copolymer and show nonterminal behavior with increasing clay content. However, the authors do not take into consideration the morphology and orientation of the block copolymer which may develop (below the ODT) during the melt blending process and the oscillatory shear experiments in both the neat and the filled triblock copolymers.

Clay−block copolymer nanocomposites have also been modeled theoretically. Lee et al.[31] performed simulations on the intercalation kinetics of short lamellar amphiphilic diblock copolymers into an organically modified clay tactoid. The authors examined the influence of various assumed interaction parameters between the clay and the two blocks copolymer components. They showed that intercalation is heavily favored in all scenarios considered. The block copolymer will intercalate the clay even when its individual block components do not intercalate as individual homopolymers, and the intercalation can occur both below and above the ODT. In another theoretical study, Groenewold and Fredrickson[32] have also performed simulations on the thermodynamic stability of fully exfoliated clay residing preferentially in one block of a lamellar diblock copolymer. Upon exfoliation and insertion into the lamellar medium, they show that the elastic interactions between particles propagate over large distances through the lamellar medium due to the large aspect ratio. Despite the long-range interactions, thermodynamic stability is observed in the cases of flexible and of rigid clay particles in the dilute and the semidilute regime, but an instability toward macrophase separation of the particles from the polymer may develop if the long-range elastic deformation forces are overcome by fluctuations due to the small elastic constants of the block copolymer melt.

These prior studies point the need for a systematic exploration of the large strain deformation behavior of a hierarchical nanocomposite system composed of a block copolymer and a layered-silicate. We have roll-cast a lamellar styrene−isoprene−styrene triblock copolymer (SIS) with various (0, 2.5, and 10 wt %) organically modified montmorillonite clay where the polymer−nanoparticle blend essentially goes through an order−disorder concentration (ODC) at room temperature during the processing operation. The resulting neat and composite films possess a uniaxial texture which allows us to study the mechanical properties and the deformation mechanism along two principal directions.

Experimental Section

Materials and Sample Preparation. Films of SIS were prepared from a commercial grade Vector 4411-D obtained from Dexco Polymers. The molecular weight of each of the PS blocks was 18 000, and the isoprene block was 44 000, giving a 45 wt % styrene. The layered-silicate used in this study was a commercial organically modified grade Cloisite 10A (C10A) supplied by Southern Clay Products. The montmorillonite is organically modified by dimethylbenzyl hydrogenated-tallow ammonium with a cation-exchange capacity (CEC) of 125

mequiv/100 g. C10A was dried in a vacuum oven at 80 °C for approximately 3−4 days to remove excess moisture. The dried C10A was then dispersed in toluene at approximately 2−3 wt % and ultrasonicated for about 1 h followed by a vigorous stirring for about 2 h. The liquid suspension is yellowish-clear. The SIS was dissolved separately in toluene forming a clear 20 wt % solution. The two solutions were then combined together with vigorous stirring and solvent was allowed to evaporate slowly until a viscous pale-yellow 30 wt % solution was achieved. Samples containing 0, 2.5, and 10 wt % C10A/SIS were prepared by static casting to produce isotropic samples. To produce oriented samples, the roll-casting technique was used in which the solution is slowly evaporated between two counterrotating cylinders.[33−35] Previous work has shown that as the solvent evaporates, the block copolymer undergoes microphase separation and the microdomains orient along the flow direction. Orientation was shown to also occur in block copolymer−homopolymer blends.[34] The roll-cast films were then dried in a vacuum oven at 120 °C for 12 h to remove final traces of the solvent as well as to improve the ordering of the block copolymer domains.

Characterization: Sample Microstructure. A Rigaku RU300 X-ray diffractometer (XRD) with Cu Kα ($\lambda = 0.154$ nm) radiation generated at 60 kV and 300 mA was used to examine the gallery height of the layered silicates before and after incorporation into the SIS. Powders of dried C10A, powders cast after ultrasonication in toluene (residual solvent present), and SIS samples incorporated with C10A were investigated. Diffraction spectra were obtained over a 2θ range of 1.5°−10° in steps of 0.02° and varying counting times to ensure good signal-to-noise ratio. The orientation of the clay layers in roll-cast samples was observed using a computer-controlled Siemens X-ray system in the wide-angle X-ray scattering (WAXS) configuration. The X-rays were generated from a rotating anode producing Cu Kα radiation operating at 40 kV and 30 mA. Data were collected using a 2D detector consisting of a pressurized xenon chamber with a wire grid assembly (512 × 512).

The microstructural changes during deformation were monitored using small-angle X-ray scattering (SAXS) at Brookhaven National Laboratory at the Time-Resolved Diffraction Facility (station X12B). A custom-built two-dimensional gas delay-line detector was used, interfaced with a real-time histogramming memory system. The sample-to-detector distance was 255 cm with $\lambda = 0.1673$ nm. Samples with dimensions of 2.6 × 1.7 × 7.5 mm were stretched in a custom-built tensile stage at a crosshead speed of approximately 3.4 mm/min. The samples were deformed in two directions relative to the texture axis and are termed parallel and perpendicular.

Transmission electron microscopy (TEM) was also used to characterize the morphology. Thin sections of roll-cast 0, 2.5, and 10 wt % C10A/SIS samples were prepared by ultramicrotomy at −100 °C and were placed above a 4% aqueous solution of osmium tetraoxide for 2 h to selectively stain the PI block. The stained sections were examined using a JEOL 200CX TEM operated at 200 keV. TEM images were Fourier transformed to provide information on the *local* order of the microdomains in the samples.

Characterization: Mechanical Properties. Samples for testing the isotropic properties were cut from the static cast films into rectangular bars. Samples to test for directional dependence of the mechanical properties were cut from roll-cast films, as shown in Figure 1. The coordinate system is as follows: the *x*-axis is the roll-cast direction, the *y*-axis is the direction normal to the film surface, and the *z*-axis is the neutral direction. The samples were cut at 0° and 90° with respect to the orientation direction. Uniaxial tensile stress−strain measurements were performed on an Instron 4501 apparatus with a crosshead speed of 5 mm/min. Data reported in the table are from averaging of at least five samples.

Results

Morphology Characterization. The lamellar spacing of the neat SIS triblock measured by SAXS is found to be approximately 28 nm. Since the volume fraction is 43% PS ($\rho_{PS} = 1.04$ g/cm^3), this approximately corresponds to PS layers of 12 nm and PI layers of 16 nm. The spacing of the neat dried C10A is approximately 1.9 nm as measured by XRD. XRD in Figure 2 shows the gallery height spacing of the as-received clay, clay cast after ultrasonication in toluene solution (residual toluene present), and the clay after incorporation into the SIS at 10% loading content. Note that a small amount of intercalation is suggested from the XRD measurements with a weak lower angle peak occurring at 3.4 nm in the 10 wt % C10A/SIS system. The 1.7 nm peak is not the second order of the 3.4 nm peak due to its much stronger intensity and much narrower width and corresponds to the first-order peak for immiscible clay tactoids. Table 1 lists in detail the measured intercalated *d* spacings of C10A in the various samples studied.

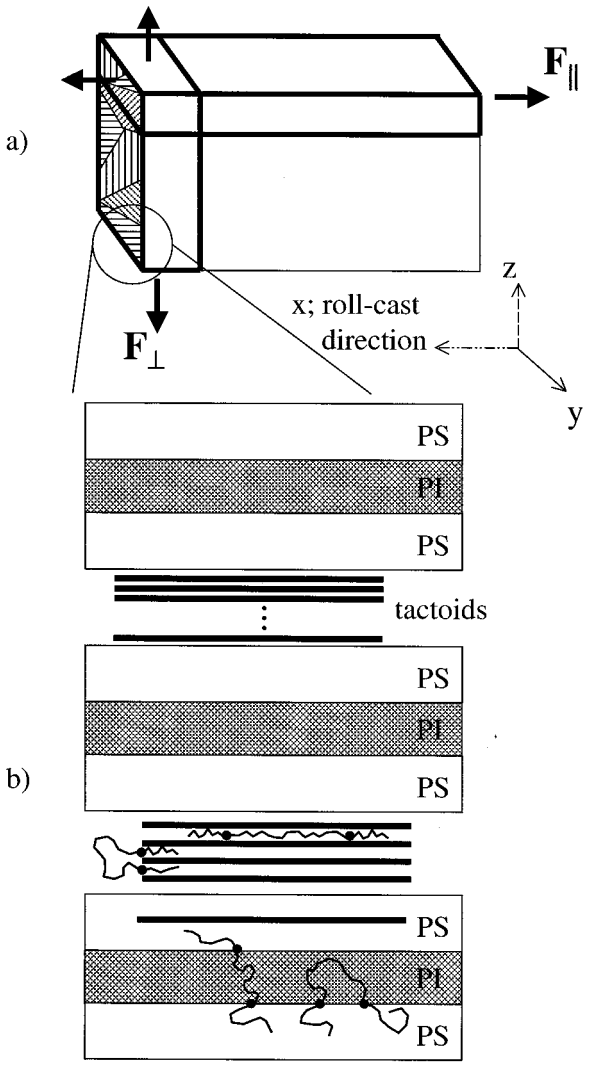

Figure 1. (a) Schematic diagram of the roll-cast samples showing the roll-cast directions and the deformatiion directions. $F_{\|}$ is referred to as the parallel direction, and $F_{\perp}$ is referred to as the perpendicular direction. Note the uniaxial orientation of the lamellar grains. (b) Magnified schematic within one grain of BCP domains, exfoliated, intercalated clay layer with possible block copolymer chain configurations, and nonintercalated clay tactoids. Block copolymer junctions are bold dots.

SAXS and the XRD measurements of simple cast 2.5 and 10 wt % C10A/SIS composites show that whereas

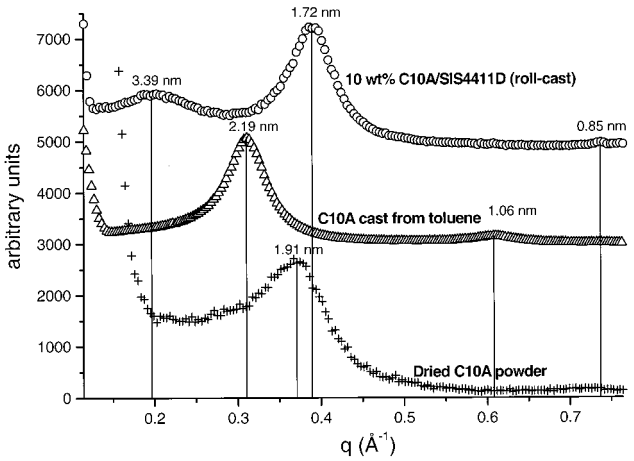

Figure 2. XRD patterns of dried C10A powder, C10A cast from toluene (residual toluene present), and C10A incorporated into SIS 4411D at 10 wt %. Smallest available slits were used to minimize parasitic scattering, and the background data collected using a glass slide were subtracted from all obtained plots. Note the increase in the peak spacings, suggesting that intercalated structures are present.

the block copolymer domain spacing is essentially unchanged, the spacing of the weak lower angle peak of C10A is now approximately 3.7 and 3.5 nm, respectively. SAXS and WAXS measurements confirm that as expected the lamellar grains as well as the layered silicates are isotropically arranged.

Roll-casting develops a preferred orientation of the lamellae as evident in the SAXS patterns taken with the beam along $\hat{y}$ for the 0, 2.5, and 10 wt % C10A filled SIS samples as shown in Figure 3a−c. For the incident beam along $\hat{x}$, the SAXS pattern is almost circularly symmetric (see Figure 3d). These two observations demonstrate the roll-cast samples display an essentially *uniaxial texture*. The lamellae are thus arranged in grains whose normals lie approximately perpendicular to the flow direction (the *x*-direction). There is however some decrease in the quality of the alignment with increasing silicate content. Figure 3e also shows the WAXS pattern of a 10 wt % C10A/SIS with the X-ray beam along $\hat{y}$ showing the preferential orientation of the silicate layers within and parallel to the lamellar morphology of the block copolymer (compare parts c and e of Figure 3).

Thus, the roll-cast nanocomposites of silicate and block copolymer are comprised of clay layers preferentially aligned parallel to the microdomain layers within the block copolymer matrix. The lamellae and the clay tactoids are both well oriented in the flow direction, and the grains containing the SIS and clay tactoids possess a uniaxial symmetry about the flow direction.

Figure 4 shows a TEM micrograph of a large lamellar grain stained with osmium tetraoxide viewing along $\hat{x}$ of the roll-cast 2.5 wt % C10A/SIS. The dark periodic layers correspond to the OsO_4-stained isoprene, and the irregular and the elongated dark regions correspond to the aligned clay layers or tactoids. The micrograph also shows a few individual clay layers that have fully exfoliated that lie preferentially within the PS layers (arrowed regions). These individual clay layers do not contribute to a scattering peak in the XRD. The inset is a low-magnification micrograph of an unstained sample (hence, all the dark regions are clay tactoids) that shows the long-range orientation of the silicate bundles with a lamellar grain. It is important to note that we have selected a large lamellar grain for edge-on viewing so that nearly all of the tactoids are also edge-on, resulting in good visualization of both the clay particles and the PS/PI layers. The area fraction of the clay in the particular region selected is somewhat above the 2.5% loading. This arises due to fluctuations in the local clay content from region to region and our selection of an area showing many clay particles. Micrographs of grains of different orientation, e.g., those in plan view viewed along the normal to the layers and clay particles, are of low contrast.

Thus, SAXS, WAXS, and TEM demonstrate that the roll-cast nanocomposites can be treated as a hierarchical anisotropic block copolymer system that contains within the structure anisotropic fillers arranged with the same orientation as the microdomain layers within micron sized grains possessing a "fiberlike" symmetry about the roll-cast direction. A microstructural schematic of the oriented roll-cast clay−BCP composite is shown in Figure 1.

Mechanical Properties. The average mechanical property values are reported in Table 1. The tensile stress−strain behavior of the isotropic static cast samples is as shown in Figure 5. Whereas the neat SIS polymer showed no signs of necking, the composites containing the layered-silicates all exhibited necking behavior. The onset of strain hardening occurred at lower strains with increasing clay content, and the modulus of the composite systems increased at higher clay loadings. The yield stress, defined as $d\sigma/d\epsilon = 0$ for samples that neck, is shown to increase while the yield strain, using a 2% offset criterion, is seen to decrease with increasing clay content. Furthermore, the rate of strain hardening, defined by $\langle d\sigma/d\epsilon = 0 \rangle$ in the strain hardening regime, is shown to increase with increasing clay content. The undulations in the stress−strain curves arise when multiple necks formed during deformation, with each drop in stress corresponding to the formation of a new neck.

The tensile stress−strain behavior of the anisotropic roll-cast samples is shown in Figures 6 and 7. When deformed along $\hat{x}$, the onset of strain hardening occurred at lower strains for samples containing higher layered-silicates content. In this direction, there is however little effect of the clay content on the modulus, yield stress, yield strain, and the rate of strain hardening. Upon unloading from 400% strain, the residual strain increases with higher clay loading. Further "healing" of the lamellar structure, measured through calipers, occurs after annealing at 120 °C in a vacuum for 2 days. The final residual strain decreases to approximately 10% and to 40% for 2.5 and 10 wt % samples, respectively.

For deformation along the normal to $\hat{x}$, the tensile modulus dramatically increases (∼2× for 2.5 wt % loading and ∼3× for 10 wt % loading) whereas no significant changes in the strain hardening behavior can be observed. Furthermore, the yield stress is seen to increase with increasing loading content and the yield strain is seen to decrease with increasing loading content as is evident in the inset to Figure 7. Necking was observed for systems that contain clay as was observed for the isotropic samples, whereas the neat roll-cast SIS samples did not exhibit necking when deformed along $\hat{z}$. Furthermore, the rate of strain hardening increases with increasing clay content, and the residual strain (measured immediately after un-

Table 1. Average Clay Layer Spacings and Mechanical Properties of the Various Nanocomposite Systems

material	*d*-spacing of C10A (nm)	Young's modulus (MPa)	yield stress (MPa)	2% offset yield strain (%)	rate of strain hardening (MPa)	residual strain (unloaded)	residual strain (annealed)
dried C10A powder	1.9						
C10A cast from toluene	2.2						
pure SIS 4411D (isotropic)		50 ± 5	2.1 ± 0.3	4.2 ± 1.3	0.7 ± 0.15	0.42 ± 0.1	0 ± 0.1
2.5 wt % C10A/SIS (isotropic)	3.7	72 ± 8	3.6 ± 0.4	5.9 ± 1.1	1.3 ± 0.20	0.57 ± 0.1	0.04 ± 0.1
10 wt % C10A/SIS (isotropic)	3.5	105 ± 6	4.6 ± 0.2	6.8 ± 1.0	3.1 ± 0.38	0.8 ± 0.1	0.32 ± 0.1
pure SIS 4411D (parallel)		153 ± 3	5.1 ± 0.2	4.4 ± 1.5	0.8 ± 0.22	0.4 ± 0.1	0.0 ± 0.1
2.5 wt % C10A/SIS (parallel)	3.7	157 ± 3	4.8 ± 0.2	4.4 ± 1.3	0.9 ± 0.14	0.6 ± 0.1	0.03 ± 0.1
10 wt % C10A/SIS (parallel)	3.4	165 ± 3	5.8 ± 0.2	4.7 ± 1.3	0.9 ± 0.10	0.8 ± 0.1	0.28 ± 0.1
pure SIS 4411D (perpendicular)		29 ± 2	1.8 ± 0.2	5.9 ± 0.8	0.7 ± 0.11	0.3 ± 0.1	0.0 ± 0.1
2.5 wt % C10A/SIS (perpendicular)	3.7	62 ± 1	3 ± 0.3	5.5 ± 1.0	0.8 ± 0.10	0.45 ± 0.1	0.0 ± 0.1
10 wt % C10A/SIS (perpendicular)	3.4	85 ± 3	3.8 ± 0.3	5.0 ± 0.9	1.0 ± 0.13	0.75 ± 0.1	0.21 ± 0.1

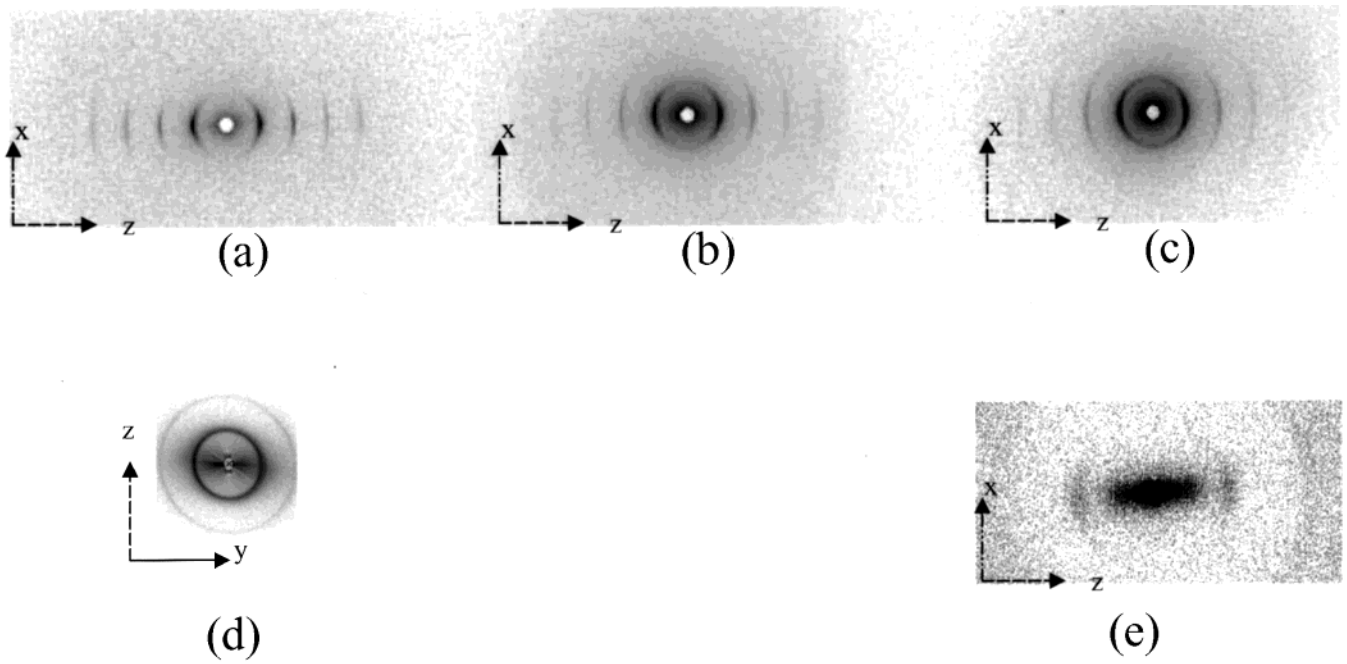

Figure 3. Roll-cast samples of (a) 0, (b) 2.5, and (c) 10 wt % C10A/SIS 4411D showing the orientation of the SIS lamellae in SAXS. Note some loss of orientation with increasing amount of the layered-silicate. The lamellar spacing is constant at approximately 28 nm. (d) SAXS pattern of 2.5 wt % C10A/SIS viewed along the roll-cast direction. Note the near isotropic nature of the block copolymer domains. (e) WAXS pattern of the 10 wt % C10A/SIS 4411D showing preferential orientation of the layered silicates.

loading from 400%) is also shown to increase. Last, annealing of the unloaded samples at 120 °C in a vacuum for 2 days resulted in near full recovery to the initial sample dimensions, the original modulus and the initial lamellar spacing (see next section).

In-Situ Deformation Studies. In-situ SAXS deformation studies were performed for the roll-cast 2.5 and 10 wt % C10A filled systems. Results obtained from the 2.5 wt % C10A filled system are presented in Figures 8 and 9 below. Generally similar behavior was observed in the 10 wt % system and is not shown.

Parallel Deformation. Parts a and b of Figure 8 correspond to SAXS patterns at 0 and 50% nominal strain, respectively, with the incident beam along the $\hat{y}$ direction. The (001) peak full width at half-maximum (fwhm), which gives a measure of the variation of the normals to the grains of lamellae oriented along the $\hat{x}$ direction, is approximately 60° for the initial sample. The loss of Bragg peaks, accompanied by an elongated, diffuse streak perpendicular to the applied force, occurs in a necked region (see Figure 8b). The local strain at the neck can be approximated as the ratio of the initial area to the necked area, A_0/A_{neck}. At 120% nominal strain, the local strain in the neck is measured to be approximately 350, 300, and 200% for 0, 2.5, and 10 wt % C10A/SIS, respectively. When the sample is unloaded from a nominal 400% strain, the sample regains some ordering of the lamellar layers as evidenced by the reappearance of a single broad, weak Bragg peak. Furthermore, the fwhm is approximately 55°, and the elliptical shape of the scattering pattern suggests that the reformed lamellar morphology has a poorer degree of orientation with the lamellar spacing varying from approximately 23 to 28 nm, depending on the orientation of the lamellar grain relative to the deformation direction.

Perpendicular Deformation. Figure 9a shows the nearly azimuthally isotropic SAXS diffraction pattern of an initial undeformed sample viewed along $\hat{x}$. Upon deformation, Figure 9b (50% strain) shows the loss of Bragg intensity along the force (vertical) direction and along the perpendicular to the force direction and the buildup of intensity at intermediate angles. There is some increased diffuse scattering near the equator

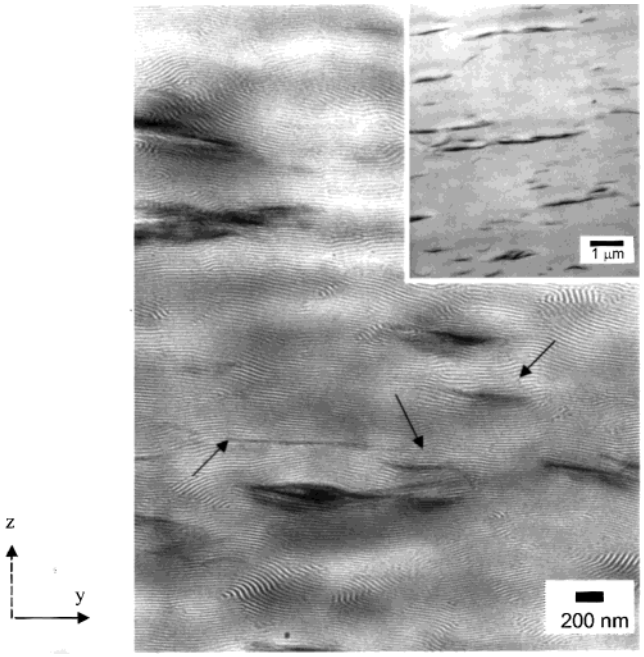

Figure 4. Bright field TEM image of a large lamellar grain in a roll-cast film of 2.5 wt % organically modified montmorillonite with 18K−44K−18K styrene−isoprene−styrene triblock. The clay particles are dispersed and oriented parallel to the oriented lamellae. The roll-casting (direction $\hat{x}$) is normal to the figure. The arrows indicate some fully exfoliated clay layers which are well aligned and located within individual PS layers.

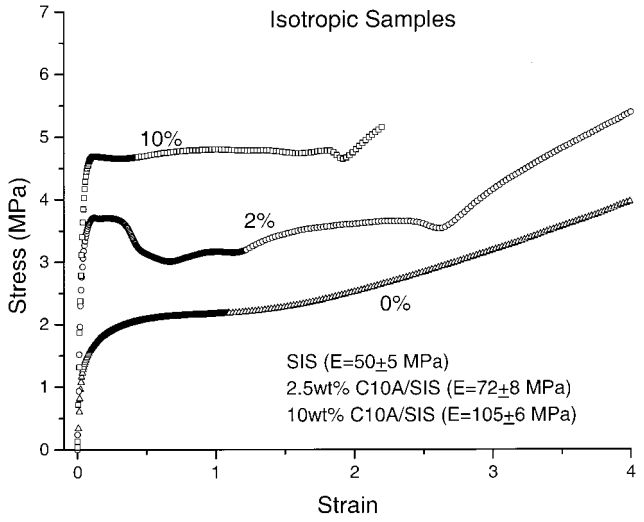

Figure 5. Stress−strain curves of static cast 0, 2.5, and 10 wt % C10A/SIS nanocomposites. Note that necking occurs in both samples containing layered-silicates. Note the increase in modulus, yield strength, and the onset of strain hardening occurs at lower strain with increasing clay content.

similar to that observed in the parallel deformation experiment. With increasing strain, a well-defined four-spot diffraction pattern appears around 100% strain (Figure 9c). The angle α between a reflection and the force direction is about 65°, and the lamellar spacing is approximately 28 nm. These four spots continually rotate away from the deformation direction at constant lamellar spacing, reaching $\alpha \approx 85°$ at 400%. When the samples are unloaded, α decreases to approximately 50° (Figure 9f). Thus, as the samples are unloaded, the chevrons do not fully relax back to the initially unkinked lamellar structure as has been observed in pure triblock

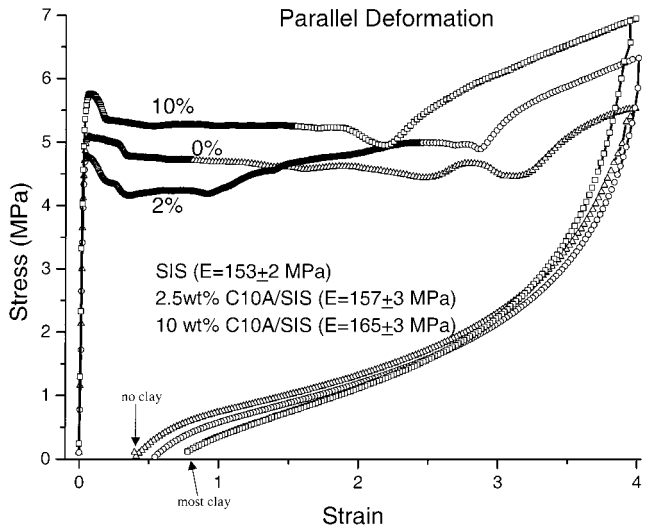

Figure 6. Stress−strain curves of 0, 2.5, and 10 wt % C10A/SIS nanocomposites deformed in the parallel ($\hat{x}$) direction. Note that necking occurs in all the samples. The modulus is nearly constant despite increasing clay loading. However, there is an earlier onset of strain hardening with increasing clay content.

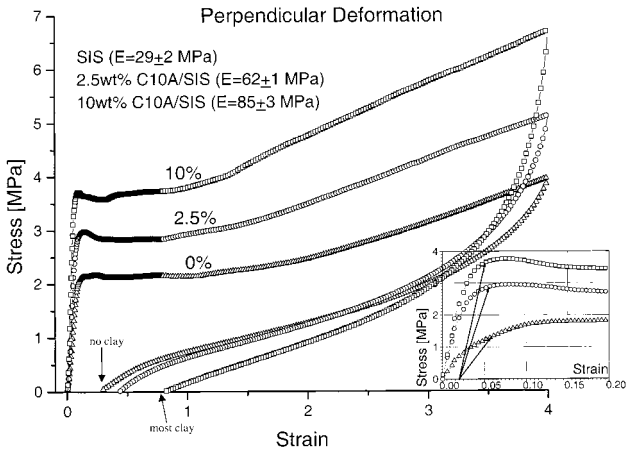

Figure 7. Stress−strain curves of of 0, 2.5, and 10 wt % C10A/SIS nanocomposites deformed in the perpendicular direction. Note that necking occurs only in the clay containing composites an not in the neat SIS. The modulus is seen to double with only 2.5 wt % C10A.

copolymer systems,[19] but only partial relaxation occurs. Cycling the system to 400% strain and back to the unloaded state does not erase the chevron morphology in the unloaded state or change the residual strain.

Figure 10 shows the TEM (edge-on view) of a large grain in an unloaded sample that was preferentially stained with OsO_4. Note the numerous chevrons that are present with $\alpha \sim 50°$ as determined from the FFT in the inset. Interestingly, the orientation of the clay tactoids, most of which have fallen out during the sample microtomy process, is now on average nearly perpendicular relative to their initial orientation in the undeformed state.

Discussion

Intercalated Clay−BCP Morphology. The schematic structural model of the roll cast nanocomposite morphology is shown in Figure 1. The system predominantly consists of nonintercalated tactoids, some intercalated material, and a minor amount of exfoliated layers. There are two general possibilities for intercala-

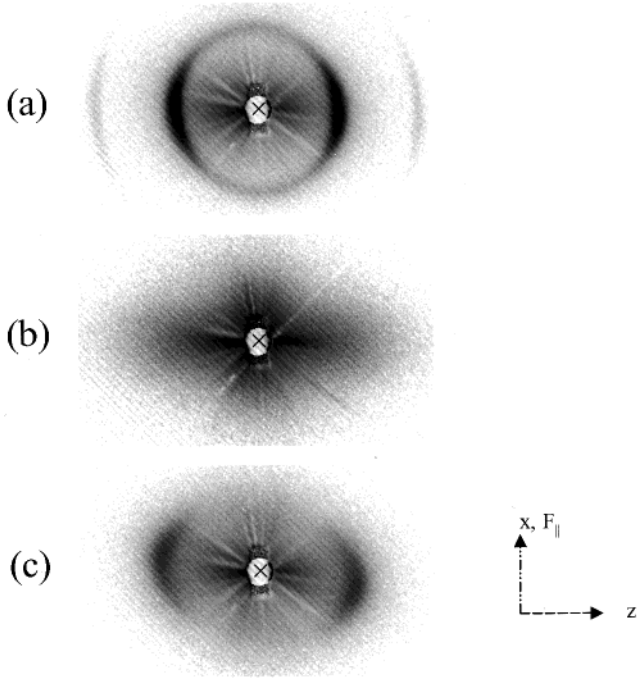

Figure 8. In-situ synchrotron scattering of 2.5 wt % C10A/SIS 4411D deformed parallel to the roll-casting direction: (a) unnecked region of the sample, (b) necked region of the sample, (c) unloaded sample showing a residual compressive strain of approximately 20%.

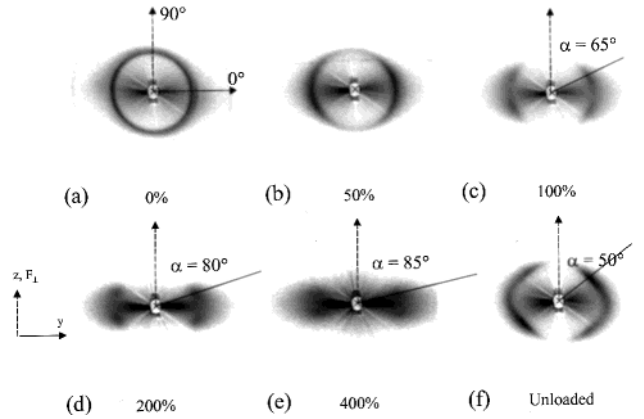

Figure 9. In-situ deformation scattering of 2.5 wt % C10A/SIS 4411D deformed perpendicular to the roll-cast direction (along $\hat{z}$) viewed along $\hat{x}$: (a) initial, (b) at 50% strain, (c) at 100% strain, (d) at 200% strain, (e) at 400% strain, and (f) unloaded state (residual strain $\approx$ 45%).

tion. First, consider only the polystyrene chains are intercalated in between the layers to avoid the unfavorable isoprene−clay interaction ("edge intercalation"). It follows then that the two styrenic end-blocks are situated near the periphery of the clay layers with the middle isoprene block remaining outside the clay layers, and the PS end-blocks can sit either in the same gallery or in different galleries. Furthermore, assume a typical C10A particle is approximately 500 nm × 500 nm (see Figure 4) and that the area coverage in the "edge intercalation" is similar to the radius of gyration of the styrene end-block, which is approximately 2 nm. Then the relative proportion of PS intercalated edge area to interior area is approximately 3%, suggesting only a very small amount of intercalation near the edge of the clay tactoids for this scenario.

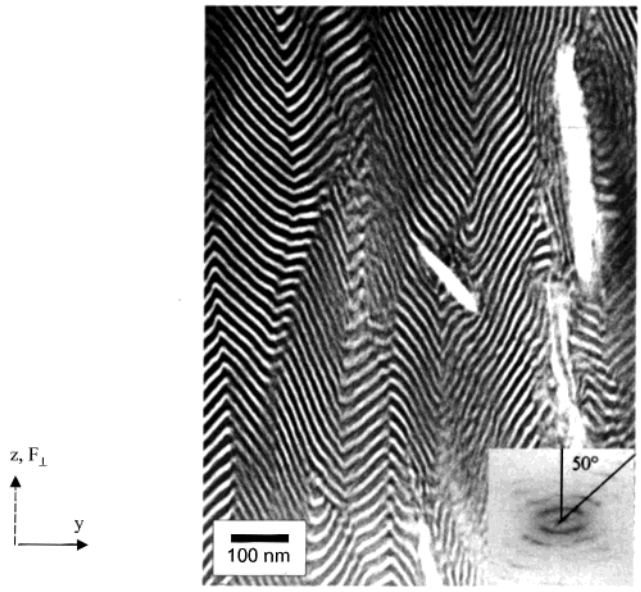

Figure 10. Bright field TEM image of roll-cast film of 2.5 wt % organically modified montmorillonite with 18K−44K−18K styrene−isoprene−styrene triblock which was stretched to 400% and unloaded (residual strain ~ 45%). The bright white regions correspond to voids where clay tactoids have fallen out during sample preparation. These are preferentially oriented perpendicular to the initial orientation direction. Inset shows fast Fourier transform (FFT) of this image area. The average value of α is approximately 50°, in good agreement with SAXS on the unloaded samples.

A second possibility is to consider that both types of blocks are incorporated into the clay layers ("full intercalation"). In fact, Ren et al.[28] and Lee et al.[31] have shown in low molecular weight styrene−isoprene diblock copolymers, and for differently modified organophilic clay, the incorporation of both blocks occurs despite the unfavorable isoprene−clay interaction. If full intercalation is present, the triblock architecture also raises the possibility that locally within the clay layers a "shielding" effect may occur by having the styrenic chains preferentially spread against the clay surfaces, allowing the isoprene block to occupy the center region and thus avoid the unfavorable interaction with the surface of the silicate layers.

The observation of the weak, broad ~3.4 nm peak and the strong, narrow 1.7 nm peak in the XRD can suggests that there is only a small amount of intercalation while the majority of the clay tactoids remain unchanged during the processing. The slight decrease in gallery spacing is attributed to the degradation and removal of the organic modifiers from the galleries during the sample annealing process.[36]

Deformation of Isotropic Polygranular Samples. The incorporation of clay particles results in a dramatic difference in the deformation behavior of the nanocomposites as compared to the neat triblocks. Modulus and yield stress increase; necking occurs along with an earlier onset of strain hardening, a higher strain hardening rate, and higher residual strains. The deformation observed in the isotropic case is due to the combined responses of grains deformed along various directions. A deconvolution of the observed effects may be understood by studying the deformation of the textured samples in the perpendicular and parallel directions.

Deformation Behavior of Anisotropic Samples. Perpendicular Deformation. The key features of

deformation along the normal to the roll-cast direction are significant increases in modulus, yield stress and residual strain, increased strain hardening rate, and neck formation. Furthermore, the formation and locking-in of a chevron texture as evidenced by the four-spot diffraction pattern in SAXS and the elongated kink boundaries imaged in TEM clearly elucidate how the morphology evolves during deformation.

SAXS patterns indicate the grains initially possess a uniaxial rotational symmetry about the *x*-axis. Thus, in the perpendicular deformation, the angle between the force axis and the lamellar normal varies from 0° to 90°.

The modulus E_θ can be expressed as

$$\frac{1}{E_\theta} = S_{33}\cos^4\theta + (2S_{13} + S_{44})\sin^2\theta\cos^2\theta + S_{11}\sin^4\theta \quad (1)$$

where $(\theta - 90)$ is the angle between the deformation direction and the lamellar normal and the S_{ij} are the four independent compliances. Index 3 refers to $\theta = 0°$ and indices 1 and 2 refer to any of the equivalent transverse directions.[37] Thus, the modulus is maximum at $\theta = 0°$ and decreases rapidly as θ increases, reaching a shallow minimum at 45°. The effective transverse modulus thus depends on the weighted average of the various lamellar orientations with respect to the direction of the applied force. For the isotropic static cast samples, the diffraction from the grains is uniformly distributed over the surface of a sphere, whereas for the uniaxial roll-cast samples, the normals to the layers in a grain are uniformly distributed over a circular ring where the thickness of ring is defined by the equatorial spread of the SAXS intensity pattern (for example, see Figure 3a for 2.5 wt % loaded sample). The greatest contribution of a grain of lamellae occurs when the force direction is orthogonal to the lamellar normal, which occurs more often in the isotropic distribution, consistent with the 1.7× higher tensile modulus of the unfilled isotropic samples compared to that of the transverse modulus of the roll-cast sample.

Additional complexities arise due to the presence of the clay. Since the tactoids align parallel to the layers in a given lamellar grain, the clay-filled nanocomposites consist of alternating stiff PS layers and rubbery PI layers with rigid clay tactoid particles. The reinforcement due to the clay is readily apparent for the 2.5% and 10% clay filled isotropic samples and particularly for uniaxial samples in perpendicular loading where the modulus increases almost a factor of 3 over the unfilled SIS.

The SAXS and TEM data allow insight into the deformation behavior of these nanocomposites. We first discuss the deformation of a neat near-single-crystal lamellar triblock copolymer reported by Cohen et al.[19,20] and then discuss the deformation behavior of our samples, in particular with respect to the SAXS scattering patterns.

For a near-single-crystal sample deformed along the lamellar normal ("perpendicular deformation"), Cohen et al.[19,20] have shown the layers start to undulate near defect sites at low strains. At higher strains the undulations fold into a chevron morphology, followed by the formation of distinct kink boundaries. The deformation was affine with the macroscopic strain, λ, simply given by $1/\cos\alpha(\lambda)$. Immediately upon unloading, the macroscopic residual strain is about 40%, and the initial lamellar period returns without noticeable residual layer strains. Annealing above the T_g of PS results in full recovery.

Cohen et al. also showed that, for single-crystal samples oriented 45° to the deformation direction, the majority of the sample responds via the rotation of the lamellar normal away from the loading direction with increasing strain. However, because of lateral forces from Poisson contraction, small portions of the layers form narrow asymmetric kink bands aligned with the kink boundaries parallel to the force direction. Upon unloading, the initial 45° orientation is returned but with somewhat poorer ordering of the lamellae.

The scattering pattern observed in Figure 9b represents the contributions from lamellae deformed at various orientations with respect to the loading direction. Because of the uniaxial symmetry, only the first quadrant of the scattering pattern needs to be considered. Those grains oriented at 45° with the lowest effective modulus respond initially to deformation by reorienting their normal toward the 0° (force) direction. After this initial response, other grains oriented in various directions respond when the critical stress to "activate" these grains has been reached. In particular, the transversely loaded lamellae begin to undulate and fold, leading to a decreased scattering along the loading direction. A four-point scattering pattern may already be embedded in Figure 9b, but the presence of strong reflections at 0° from the parallel loaded lamellae masks this observation. This suggests that the layer fragmentation, as evidenced in the parallel deformation, has not yet occurred at this strain (50%), which is significantly higher than the strain at the onset of necking in the parallel deformation (~5%; see Figure 6). The macroscopic necking phenomenon observed near 6−8% strain in the perpendicular deformation is probably purely due to the presence of the clay that causes local stress concentrations around the clay tactoids as necking is an inhomogeneous yielding phenomenon observed when a maximum load is followed by nonuniform or localized deformation.[38]

Upon further deformation, the critical stress to fragment those lamellae with normals at 0° is locally exceeded, and the diffuse scattering oriented principally along 0° can be attributed to the breakup of the PS layers oriented parallel to the deformation direction. The loss of the scattering along the 90° and 0° directions allows easy identification of the chevron pattern with $\alpha \approx 65°$. At higher deformation, the layer normals continually rotate away from the deformation direction without appreciable changes in the lamellar spacing as shown in Figure 9c−e where the strain reaches 400% and $\alpha \approx 85°$.

Our results show that the measured α is always somewhat larger than the value expected by assuming an affine deformation model during deformation. For example, at 100% strain $\alpha = 65°$ vs 60°, at 200% strain $\alpha = 80°$ vs 70°, and at 400% strain $\alpha = 85°$ vs 78°. This suggests that presence of the clay causes the rotating layers to effectively experience a larger strain than the overall average sample strain.

The TEM micrographs suggest that, during deformation at high strains, not only do the BCP lamellar normals continually rotate away from the deformation direction but the clay layer normals also rotate away from the deformation direction. Upon unloading, the elastic restoring force of the isoprene blocks causes the

lamellae to reorient back toward their initial orientations, but the clay tactoids remain aligned essentially along the initial deformation direction, restricting the relaxation of the chevrons. This "locking" force induced by the presence of the clay layers accounts for the observed increases in the residual strain with increasing loading content.

Parallel Deformation. The key features of deformation along the roll-cast direction are the apparent insensitivity in modulus and strain hardening rate with respect to the clay content, but the earlier onset of strain hardening and increased residual strains with higher clay loading content. Furthermore, the distribution in the lamellar spacings also illustrates the effect of the clay particles in the unloading behavior of these nanocomposites.

Previous work by Cohen et al.[19] showed, under parallel deformation, the PS layers initially take up most of the load, followed by a fragmentation of the PS domains leading to the necking phenomenon. This latter process leads to void scattering as evidenced in the SAXS patterns as shown in Figure 8b. The onset of strain hardening is attributed to further fragmentation of the glassy remnants.

The apparent insensitivity of the tensile modulus for deformation along the $\hat{z}$ direction to the amount of clay loading is indicative of the fact that, as in a pure triblock copolymer system, most of the initial force is taken up by the PS glassy domains. Necking occurs at relatively constant strain for the various loading contents.

Interestingly, the yield stress is slightly less at 2.5 wt % loading compared to the 0% and 10% samples. This may simply be the result of surface imperfections of the clay filled tensile samples, causing initiation of necking at lower stresses. At necking, diffuse scattering arises in the necked region, whereas the unnecked portions of the sample still show the original lamellar SAXS pattern, suggesting the breakup of the glassy PS layers occurs along with the formation of voids in the necked regions as has been observed in pure triblock copolymers. The earlier onset of strain hardening in parallel loading with increasing loading content of clay indicates an earlier fragmentation of the glassy PS remnants. This suggests that the clay tactoids may induce stress concentrations in the SIS around them, leading to PS fragmentation and earlier strain hardening behavior. However, the apparent insensitivity of the strain hardening rate suggests that, after the final PS fragmentation, the strain hardening is purely dominated by the stretching of the rubbery isoprene domains.

Upon unloading, the retractile forces, which are dominantly from the stretched rubber chains, are competing not only with the back stresses of the plastically deformed PS layers but also with the clay layers that are present in the sample. This leads to a larger residual strain and a higher degree of disorder upon unloading as shown by the distribution in lamellar spacing and the elliptical shape of the SAXS scattering pattern.

Future Work. This investigation raises questions as to the exact nature of the block copolymer chains confined between clay layers. Furthermore, processing to achieve a single-crystal texture of the block copolymer morphology will allow further elucidation of the importance of grain compatibility constraints and is currently under investigation. Last, the effect of fully exfoliated clay sequestered preferentially in one block copolymer domain on mechanical and transport behavior as opposed to the small amount of intercalated and dominantly immiscible tactoids of the present work is of significant interest and is actively being pursued.

Conclusion

Roll-casting has been used to produce highly oriented clay−triblock copolymer nanocomposites. Observation of the microstructure with XRD and TEM shows that only a small amount of partial intercalation and exfoliation has occurred. These nanocomposites exhibit dramatic differences in mechanical behavior from that of the neat triblock copolymer. Static cast, isotropic polygranular samples exhibit increases in modulus and yield stress, necking phenomenon, earlier onset of strain hardening, higher strain hardening rate, and higher residual strains as the clay content is increased. Roll-cast samples possessing a uniaxial symmetry of the lamellar grains have the layered-silicates well oriented in the flow direction and parallel to the block copolymer layers in a given grain. These anisotropic samples were deformed in directions parallel and perpendicular to the roll cast direction. In the perpendicular deformation, modulus, yield stress, strain hardening rate, and residual strain are shown to increase with increasing clay content. The unloading of a highly deformed sample shows the chevron morphology has been partially locked in due to the presence of the rigid clay particles. The parallel deformation studies suggest that the effect of the clay particles is dominant in the higher strain deformation and unloading regions as evidenced by earlier onset of strain hardening behavior and the increased residual strain.

The understanding of the evolution of the anisotropic morphology during deformation is generally applicable to many nanocomposite studies. These results illustrate the importance of considering the symmetry of the nanocomposite system that may be developed during processing operations. Thus, future studies should be increasingly aware of the effects of global orientation to the mechanical properties of the nanocomposites investigated. Furthermore, the improvements in the mechanical properties of a widely used SIS thermoplastic elastomer should allow new areas of application for these materials.

Acknowledgment. We thank Dr. Ramon Albalak, who has provided the initial inspiration for this project. We also thank Dr. Richard Vaia, who has provided numerous and insightful advice in the work. Prof. Yachin Cohen has also provided valuable discussions, and the efforts of Albert Liu in producing roll cast samples are greatly appreciated. We also thank Dr. M. Capel at Brookhaven National Laboratory for his assistance in the beamline. We also thank the Air Force for the funding of this research under Grant F49620-01-1-0447.

References and Notes

(1) Giannelis, E. P. *Adv. Mater.* **1996**, *8*, 29−35.
(2) Messersmith, P. B.; Giannelis, E. P. *Chem. Mater.* **1993**, *5*, 1064−1066.
(3) Messersmith, P. B.; Giannelis, E. P. *J. Polym. Sci., Part A: Polym. Chem.* **1995**, *33*, 1047−1057.
(4) Giannelis, E. P.; Krishnamoorti, R.; Manias, E. *Polym. Confined Environ.* **1999**, *138*, 107−147.
(5) Krishnamoorti, R.; Vaia, R. A.; Giannelis, E. P. *Chem. Mater.* **1996**, *8*, 1728−1734.
(6) Usuki, A.; Kojima, Y.; Kawasumi, M.; Okada, A.; Fukushima, Y.; Kurauchi, T.; Kamigaito, O. *J. Mater. Res.* **1993**, *8*, 1179−1184.

(7) Kojima, Y.; Usuki, A.; Kawasumi, M.; Okada, A.; Fukushima, Y.; Kurauchi, T.; Kamigaito, O. *J. Mater. Res.* **1993**, *8*, 1185−1189.
(8) Yano, K.; Usuki, A.; Okada, A.; Kurauchi, T.; Kamigaito, O. *J. Polym. Sci., Part A: Polym. Chem.* **1993**, *31*, 2493−2498.
(9) Folkes, M. J., Ed. *Processing, Structure and Properties of Block Copolymers;* Elsevier Applied Science: New York, 1985.
(10) Holden, G., Legge, N. R., Quirk, R. P., Schroeder, H. E., Eds. *Thermoplastic Elastomers,* 2nd ed.; Hanser Publishers: New York, 1996.
(11) Honeker, C. C.; Thomas, E. L. *Chem. Mater.* **1996**, *8*, 1702−1714.
(12) Dair, B. J.; Avgeropoulos, A.; Hadjichristidis, N.; Capel, M.; Thomas, E. L. *Polymer* **2000**, *41*, 6231−6236.
(13) Prasman, E.; Thomas, E. L. *J. Polym. Sci., Part B: Polym. Phys.* **1998**, *36*, 1625−1636.
(14) Honeker, C. C.; Thomas, E. L.; Albalak, R. J.; Hajduk, D. A.; Gruner, S. M.; Capel, M. C. *Macromolecules* **2000**, *33*, 9395−9406.
(15) Honeker, C. C.; Thomas, E. L. *Macromolecules* **2000**, *33*, 9407−9417.
(16) Chen, Z. R.; Kornfield, J. A.; Smith, S. D.; Grothaus, J. T.; Satkowski, M. M. *Science* **1997**, *277*, 1248−1253.
(17) Kofinas, P.; Cohen, R. E. *Macromolecules* **1995**, *28*, 336−343.
(18) Keller, A.; Pedemonte, E.; Willmouth, F. M. *Nature (London)* **1970**, *225*, 538−539.
(19) Cohen, Y.; Albalak, R. J.; Dair, B. J.; Capel, M. S.; Thomas, E. L. *Macromolecules* **2000**, *33*, 6502−6516.
(20) Cohen, Y.; Brinkmann, M.; Thomas, E. L. *J. Chem. Phys.* **2001**, *114*, 984−992.
(21) Hadziioannou, G.; Mathis, A.; Skoulios, A. *Colloid Polym. Sci.* **1979**, *257*, 136−139.
(22) Hadziioannou, G.; Mathis, A.; Skoulios, A. *Colloid Polym. Sci.* **1979**, *257*, 15−22.
(23) Hadziioannou, G.; Mathis, A.; Skoulios, A. *Colloid Polym. Sci.* **1979**, *257*, 337−343.
(24) Hadziioannou, G.; Mathis, A.; Skoulios, A. *Colloid Polym. Sci.* **1979**, *257*, 344−350.
(25) Keller, A.; Dlugosz, J.; Folkes, M. J.; Pedemonte, E.; Scalisi, F. P.; Willmouth, F. M. *J. Phys., Colloq. C5* **1971**, *32*, 295−300.
(26) Laus, M.; Francescangeli, O.; Sandrolini, F. *J. Mater. Res.* **1997**, *12*, 3134−3139.
(27) Galanti, A.; Laus, M.; Fiorini, M. *Kautschuk Gummi Kunststoffe* **1999**, *52*, 21−25.
(28) Ren, J. X.; Silva, A. S.; Krishnamoorti, R. *Macromolecules* **2000**, *33*, 3739−3746.
(29) Dumitru, P.; Lees, G. C.; Liauw, C. M.; Rothon, R. N. *Macromol. Symp.* **2001**, *170*, 213−220.
(30) Lim, Y. T.; Park, O. O. *Korean J. Chem. Eng.* **2001**, *18*, 21−25.
(31) Lee, J. Y.; Baljon, A. R. C.; Sogah, D. Y.; Loring, R. F. *J. Chem. Phys.* **2000**, *112*, 9112−9119.
(32) Groenewold, J.; Fredrickson, G. H. *Eur. Phys. J. E* **2001**, *5*, 171−182.
(33) Albalak, R. J.; Thomas, E. L. *J. Polym. Sci., Part B: Polym. Phys.* **1993**, *31*, 37−46.
(34) Albalak, R. J.; Thomas, E. L. *J. Polym. Sci., Part B: Polym. Phys.* **1994**, *32*, 341−350.
(35) Albalak, R. J.; Thomas, E. L.; Capel, M. S. *Polymer* **1997**, *38*, 3819−3825.
(36) Xie, W.; Gao, Z. M.; Pan, W. P.; Hunter, D.; Singh, A.; Vaia, R. *Chem. Mater.* **2001**, *13*, 2979−2990.
(37) Allan, P.; Arridge, R. G. C.; Ehtaiatkar, F.; Folkes, M. J. *J. Phys. D* **1991**, *24*, 1381−1390.
(38) McClintock, F. A.; Argon, A. S. *Mechanical Behavior of Materials*; Addison-Wesley: Reading, MA, 1966.

MA012210H